

# Deep Phase Coded Image Prior

Nimrod Shabtay<sup>1</sup>, Eli Schwartz<sup>1,2</sup>, and Raja Giryes<sup>1</sup>  
<sup>1</sup>Tel-Aviv University, <sup>2</sup> IBM Research

**Abstract**—Phase-coded imaging is a computational imaging method designed to tackle tasks such as passive depth estimation and extended depth of field (EDOF) using depth cues inserted during image capture. Most of the current deep learning-based methods for depth estimation or all-in-focus imaging require a training dataset with high-quality depth maps and an optimal focus point at infinity for all-in-focus images. Such datasets are difficult to create, usually synthetic, and require external graphic programs. We propose a new method named "Deep Phase Coded Image Prior" (DPCIP) for jointly recovering the depth map and all-in-focus image from a coded-phase image using solely the captured image and the optical information of the imaging system. Our approach does not depend on any specific dataset and surpasses prior supervised techniques utilizing the same imaging system. This improvement is achieved through the utilization of a problem formulation based on implicit neural representation (INR) and deep image prior (DIP). Due to our zero-shot method, we overcome the barrier of acquiring accurate ground-truth data of depth maps and all-in-focus images for each new phase-coded system introduced. This allows focusing mainly on developing the imaging system, and not on ground-truth data collection.

**Index Terms**—Phase-coded Imaging, Physics-based Rendering, Neural Rendering, Deep Image Prior



## 1 INTRODUCTION

PHASE coded imaging is a method in computational imaging, where a camera is equipped with an optical phase mask that provides unambiguous depth-related color characteristics for the captured image. While single-image passive depth estimation is an ill-posed problem, in phase-coded imaging, a phase mask is designed to create a different defocus blur for each color channel of the image. The depth cues, encoded by the phase mask, can later be decoded by a deep neural network for passive depth estimation or extended depth-of-field.

Prior works decode depth cues via a supervised learning approach, where a synthetic dataset with accurate depth maps and all-in-focus images is used, and a neural network is trained to extract the depth map and/or all-in-focus image from the blurred (coded) image. A major drawback of these methods is the need for a large and accurate dataset for training. Capturing such a dataset can be quite complex and may necessitate the use of external sensors or graphic rendering software.

Another issue is generalization, namely, a deep learning model trained on synthetic data may not generalize well to real-world data. Moreover, even a model trained on real-world data might suffer from a domain shift between the training and test sets.

To address the aforementioned limitations, we propose a new approach inspired by prior image restoration techniques utilizing Deep Image Prior [1]. We formulate the tasks of single-image passive depth estimation and extraction of all-in-focus images as a single inverse problem. An implicit generator with an input code is optimized to jointly create an all-in-focus image and a depth map. The loss function of the generator relies on a Differential Camera Model (DCM) that simulates phase-coded imaging from a given depth map and all-in-focus image. Thus, our loss term compares the input phase-coded image to the one generated by the DCM based on neural network reconstruction. Note

that the learning process is end-to-end. Thus, the gradients propagate all the way back to the generator to improve the mapping between the input code and the reconstructed depth map and all-in-focus image such that the DCM output matches the input. At the end of the learning process, we discard the output and just keep the depth map and an all-in-focus RGB image. Figure 1 illustrates this process.

**Contribution.** Our contributions may be summarized as (i) proposing a method to extract both depth estimation and all-in-focus images in a zero-shot manner using a known DCM, which reduces the need to capture a curated dataset for training; and (ii) outperforming prior works trained in a supervised fashion for the same imaging system.

## 2 RELATED WORK

### 2.1 Coded Aperture Imaging

Coded aperture imaging systems employ dedicated optical masks to encode light. Such imaging can decode and extract visual cues in order to reconstruct a passive depth estimation of the acquired image. Levin et al. [2] use an amplitude-coded mask such that objects at different depths exhibit a distinctive spectral structure. Haim et al. [3] proposed a ring phase mask to generate depth-dependent PSF filters for encoding the depth cues. They proposed a fully-convolutional neural network to learn the decoding process to generate the depth map. A follow-up work by Gil et al. [4] leverages the encoding process in a stereo vision setup where conventional cameras fail. Chang et al. [5] proposed a depth-dependent image formation where a neural network learns to extract a depth map from a simulated acquired image produced from an all-in-focus image, a binned depth map and the lens parameters. Wu et al. [6] proposed an end-to-end architecture consisting of two parts: An optical layer simulates depth-dependent PSFs given a learnable phase

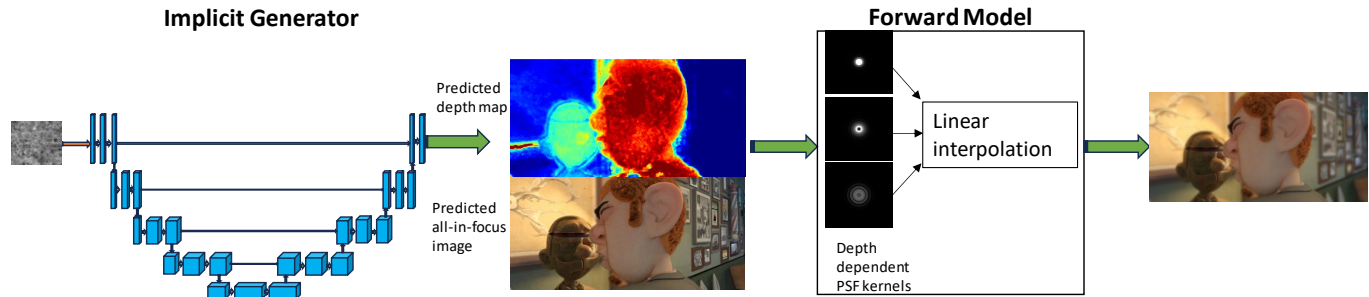


Fig. 1. **System overview.** We follow a neural field flow, where an implicit generator first maps the encoded input image into reconstruction representations (in our case an all-in-focus image and a depth map). In the second part, A Differential Camera Model (DCM), a simulated differential forward (acquisition) process of a phased-coded imaging system, provides the acquired image. Both parameters in the generation part, and in the DCM part, are optimized based on the loss defined between the estimated phase-coded image and the input image.

mask, and a reconstruction network, which estimates depth from the coded image.

Another line of work aims to recover an extended depth of field (EDOF) in order to reconstruct an all-in-focus image from the acquired image. Elmalem et al. [7] proposed to use a ring mask with a depth-dependent PSF function and a neural network to recover the depth cues and the all-in-focus image. Akpinar et al. [8] employed wavefront coding via a diffractive optical element (DOE) and a neural network for deblurring in an end-to-end learning process. Gkioulekas et al. [9] used a dual pixel camera and a pre-defined per depth calibration kernel set, to construct a multi-depth representation for extracting the all-in-focus image and the depth map simultaneously. Sitzmann et al. [10] constructed a joint optimization system composed of an optical part and a reconstruction part to simulate a real image acquisition for various image processing tasks such as super-resolution and extended depth of field. In addition, Yosef et al. [11] proposed to use the coding in the temporal axis instead of the depth axis to reconstruct video from a coded motion blur. An important common property of previous works is the need to create a dedicated dataset for training the reconstruction module, where in our approach we apply a self-supervised scheme consisting only of a single input image, eliminating the cumbersome preliminary step of constructing a dedicated dataset.

## 2.2 Deep Image Prior

Deep Image Prior (DIP) [1] showed that a convolutional neural network (CNN) can recover a clean image from a degraded image in the optimization process of mapping random noise to a degraded image. The power of DIP is shown for several key image restoration tasks such as denoising, super-resolution, and inpainting. DIP was extended to various applications. DoubleDIP [12] introduced a system composed of several DIP networks, where each learns one component of the image such that their sum is the original image. It has been used for image dehazing and foreground/background segmentation. SelfDeblur [13] performed blind image deblurring by simultaneously recovering a sharp image and the corresponding blur kernel using DIP. In the realm of medical imaging, various studies have endeavored to harness the potential of image priors for the reconstruction of PET images [14], [15], [16], [17].

Alternative approaches have sought to enhance the efficacy of image priors through modifications and additions to the original configuration. Mataev et al. [18] and Fermanian et al. [19] employed a combination of DIP and the plug-and-play framework to enhance DIP’s performance across multiple inverse problems. In other domains, Kurniawan et al. [20] introduced a demosaicing method based on DIP, while Chen et al. [21] proposed a neural architecture search guided by DIP principles. Recently, Shabtay et al. [22] demonstrated the connection between DIP and implicit neural representation (INR). The connection between DIP and INR inspired the formulation of our reconstruction method as a self-supervised system consisting of a DIP generator and a DCM.

## 2.3 Implicit Neural Representation

Implicit neural representation is an area of research that studies the abilities of neural networks to map input coordinates to target values. This includes 2D images, 3D shapes, SDF maps and many more. It was demonstrated in [23] that representing the input coordinates as Fourier-features with a tuneable bandwidth enables a simple MLP to generate complex target domains such as images and 3D shapes while preserving their high-level details. In Neural Radiance Fields (NeRF) [24], implicit functions with Fourier features are used for synthesizing novel views of a 3D scene from sparse 2D images. SIREN [25] showed that by changing the activation function of a simple MLP from the frequently used ReLU to a periodic activation (for example a sine activation), the network can represent the spatial and temporal derivatives using a simple input grid to successfully recover a wide range of target domains (images, videos, 3D surfaces, etc.). Following NeRF, improvements were proposed [26], [27], [28] in terms of convergence speed compared to the original NeRF by utilizing a structure for the implicit model. Methods were also proposed [29], [30], [31] to tackle the scaling and aliasing problems that the original NeRF suffered from. Yu et al. [32] suggested a method to reduce the need for many calibrated images from sparse views as supervision for NeRF. Mildenhall et al. [33] suggested a method for rendering the raw images before the ISP in order to achieve much wider rendering abilities such as control on tone mapping. It was also proposed [34] that Gaussian activation can perform better than sine activation while

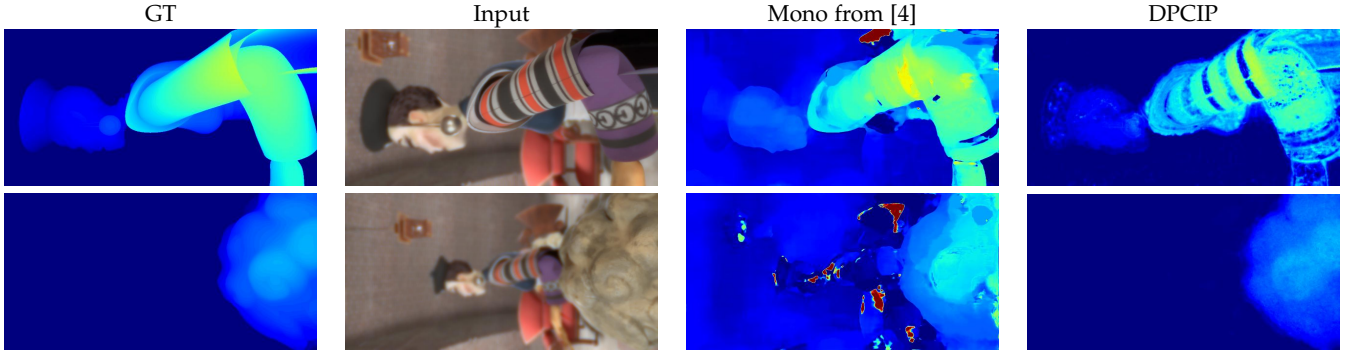


Fig. 2. **A qualitative comparison of depth map estimation** reveals that our method generates significantly more precise depth maps compared to the mono network from [4], which tends to excessively smooth the estimated maps, resulting in lower accuracy. Note that the depths are clipped to the physical range of the imaging system.

having the property of being continuous everywhere and at every derivative. SAPE [35] and BACON [36] demonstrate how a combination of a coordinate network along with a limitation of its frequency spectrum can achieve a multi-scale representation of the target domain.

### 3 DEEP PHASE CODED IMAGE PRIOR

We consider an imaging system capable of extracting simultaneously an all-in-focus RGB image and a pixel-level depth map with a single image capture. Our goal is to achieve single image depth estimation and extended depth of field (EDOF) simultaneously relying solely on the captured image without any training data. We achieve this via end-to-end joint optimization of a generation part (a U-Net shaped neural network) and a forward process part, namely, a differentiable approximation of the acquisition process of the phase-coded imaging system - DCM in short.

As shown in Figure 1 We formulate our problem as an implicit neural representation problem where our system is composed of two major components: The first one is an implicit generator based on the model introduced in DIP [1]. It is an encoder-decoder model such that the encoder has 5 levels and each level has 2 convolutional layers with a depth of 128 and the downsampling between the levels is done by stride. The decoder has also 5 levels with 2 convolutional layers with a depth of 128 followed by bilinear upsampling. At each level the model has skip connections as a convolutional layer with a depth of 16. This creates a generator whose learnable parameter is the mapping between an input code and a pair consisting of an

all-in-focus image and a pixel-level depth map. The second component is a differentiable simulation of the phase-coded optical imaging (DCM). Given a pair of an all-in-focus image and a depth map, it generates the acquired image from a phase-coded imaging system.

We simulate the coded-phase acquisition process as done in [3], [7], i.e., assuming the optical parameters are known (lens parameters and the focus point), we can recover the out of focus (OOF) condition (denoted as  $\psi$ ) using the following equation:

$$\psi = \frac{\pi R^2}{\lambda} \left( \frac{1}{z_0} + \frac{1}{z_{img}} - \frac{1}{f} \right) = \frac{\pi R^2}{\lambda} \left( \frac{1}{z_{img}} - \frac{1}{z_i} \right) = \frac{\pi R^2}{\lambda} \left( \frac{1}{z_0} - \frac{1}{z_n} \right), \quad (1)$$

where  $R$  is the radius of the exit pupil (circular aperture is assumed),  $\lambda$  is the illumination wavelength,  $z_{img}$  is the sensor plane location for an object at a nominal position  $z_n$ , and  $z_i$  is the ideal location for an image plane with respect to an object at location  $z_0$ .

From Eq. 1 we can derive that a focused object is located at  $\psi = 0$ , and an out of focus object will be located at other values of  $\psi$ .  $\psi$  ranges between  $[-4, 10]$ . With the knowledge of the focus point and the recovered  $\psi$  values for each pixel, we can recover the absolute depth for each pixel in the scene.

Our method and simulations are based on [3], [7], where we have a ring mask with pre-defined depth-dependent PSF kernels. Since the acquisition process is not differentiable, we used a differentiable approximation, in a coarse to fine manner. Instead of creating a mask that corresponds to a particular depth and convolving the specific depth with the associated pre-calculated PSF kernels, inspired by [5], [9], our DCM first creates several acquired images from a fixed set of depths ( $\psi$ ) values and then linearly interpolates each pixel with the closest depth-dependent blur images.

The differentiable variant allows us to optimize the whole system in a self-supervised end-to-end manner, where the generator first maps the input encoding to a pair of an all-in-focus image and a pixel-level depth map that are fed as inputs to the DCM in order to reproduce the acquired image taken by the camera. The joint optimization of producing both an all-in-focus image and a pixel-level depth map forces an alignment between them and yields better results compared to previous works where a model was trained to produce just a depth map or just an all-in-focus image.

TABLE 1

**A quantitative comparison of depth estimation, results are depth RMSE error [m] ( $\downarrow$ ).** Our method outperforms the mono network from [4] in depth estimation by 2 orders of magnitude on the same imaging system, even though the Monocular depth estimation network from [4] was trained in a supervised manner on the same dataset, this is likely due to the fact that dataset is small and the model is prone to overfitting.

	Supervised Mono from [4]	0-shot DPCIP
WuManchu	0.1639	<b>0.0003</b>

To optimize our neural network weights to map a coded input to pixel values we used the non differential acquisition simulation to produce coded-phase images to act as our supervision. Our objective function is to minimize the difference between a given image and the forward process output. Similarly to [13], we first use L2 as our reconstruction loss and switch to SSIM [37] after a fixed number of iterations. We can formulate our objective as follows:

$$\theta^* = \underset{x}{\operatorname{argmin}} \ell(h(f_\theta(z)) - y), \quad (2)$$

where  $h$  is the DCM,  $f_\theta$  is the implicit model and  $z$  is the encoded input.  $y$  is the blurry image acquired by our coded phase imaging system. We evaluate our method both for PSNR and SSIM for the all-in-focus images and the mean error in meters for the depth maps.

## 4 EXPERIMENTAL RESULTS

We conduct a series of experiments, both in simulation and on real-world examples using a dedicated phase-coded camera. We show only qualitative results on real-world image due to lack of ground-truth. Thus, for quantitative comparison and evaluation of our method we focused on simulated data with accurate ground-truth. Unless stated otherwise, we used a U-net model as described in Section 3. We trained with Adam optimizer [38], with 0.01 learning rate. We switched the reconstruction loss from L2 to SSIM after 500 iterations.

### 4.1 Simulation Results

To evaluate the performance of our method quantitatively both in terms of depth estimation and all-in-focus image reconstruction, we first perform an evaluation on a simulated dataset, namely, ‘TAUAgent’ dataset<sup>1</sup> [4]. The Agent dataset consists of a total of 530 images from five synthetic scenes created using the ‘Blender’ computer graphics software (named ‘City’, ‘Headbutt’, ‘Sitting’, ‘WallSlam’, ‘WuManchu’). Each scene consists of a ground-truth low-noise all-in-focus image, along with its corresponding pixel-wise accurate depth map. Such data enables an exact depth-dependent imaging simulation, with the corresponding depth of focus (DOF) effects. In contrast to prior works [3], [4], [7], we do not use the ‘ground-truth’ data from the Agent dataset in our optimization. We only use the acquired coded images produced by the camera simulation. The all-in-focus GT images and the GT depth maps are only used to evaluate the performance of our method. For the all-in-focus evaluation, we used PSNR and SSIM, while for the depth estimation, we used average error in meters (as done in [3], [4]). To make a fair comparison we simulate the imaging with the same optical parameters as done in [3], [4], [7].

Note that a crucial disadvantage of previous works is the high dependency on a large and high-quality dataset for successful learning. High-quality datasets like the ‘agent’ dataset are usually small and cumbersome to collect, thus, making the learning much more challenging. In contrast to them, our Deep Phased implicit representation reduces this constraint since we explicitly incorporate the DCM into the

learning scheme. Thus, we can extract both the all-in-focus RGB image and the pixel-level depth map from a single captured image.

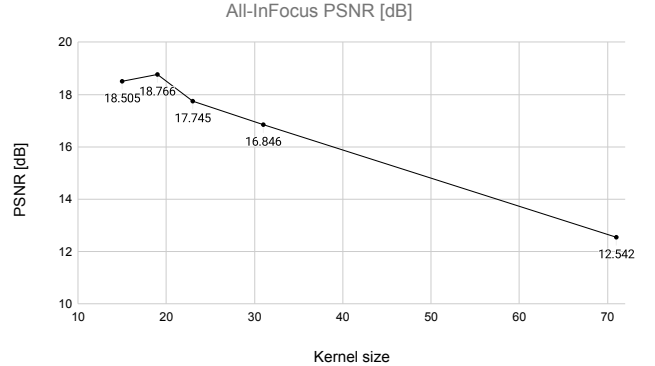


Fig. 4. **Blind image deblurring as a function of the kernel size.** The graph shows the average performance on a subset of samples to choose the best kernel size for Neural deblurring on the dataset. We can see that as the kernel size drops the performance improves, up to a certain level where the loss of deblurring signal is too large.

We took a subset of 110 images (namely, ‘agent subset’) from the scenes mentioned above to evaluate the performance on several tasks namely passive depth estimation, image reconstruction, and image deblurring. Lastly, we also show the effect of the implicit generator on the performance of the mentioned tasks.

#### 4.1.1 Passive Depth Estimation

To assess our method’s performance in passive depth estimation we compared ourselves to the Monocular depth estimation network for phase coded imaging from [4] which built upon the same phase-coded imaging system. We also followed the same optical parameters to produce the same acquired images. The evaluation was done on the relevant part of the ‘agent subset’ (‘WuManchu’ scene) that was not used for training [4]. Table 1 shows a quantitative comparison in terms of RMSE error in meters. Visual results can be found in Figures 2 ,7. Overall, our method outperformed mono network by two orders of magnitude and effectively managed to produce an accurate pixel-level depth map solely from a given captured image.

TABLE 2  
**A quantitative comparison of for image reconstruction (PSNR [dB] / SSIM).** Our method outperforms the existing supervised baseline significantly. The PSNR average improvement of our method is  $\sim 5dB$ .

Dataset	Supervised Baseline [7]	0-shot DPCIP
City	24.01/0.65	<b>29.73/0.91</b>
Headbutt	28.54/0.92	<b>31.28/0.94</b>
Sitting	26.12/0.81	<b>30.04/0.91</b>
WallSlam	26.94/0.87	<b>31.45/0.93</b>
WuManchu	23.67/0.71	<b>30.86/0.93</b>

1. <https://www.cs.toronto.edu/harel/TAUAgent/home.html>



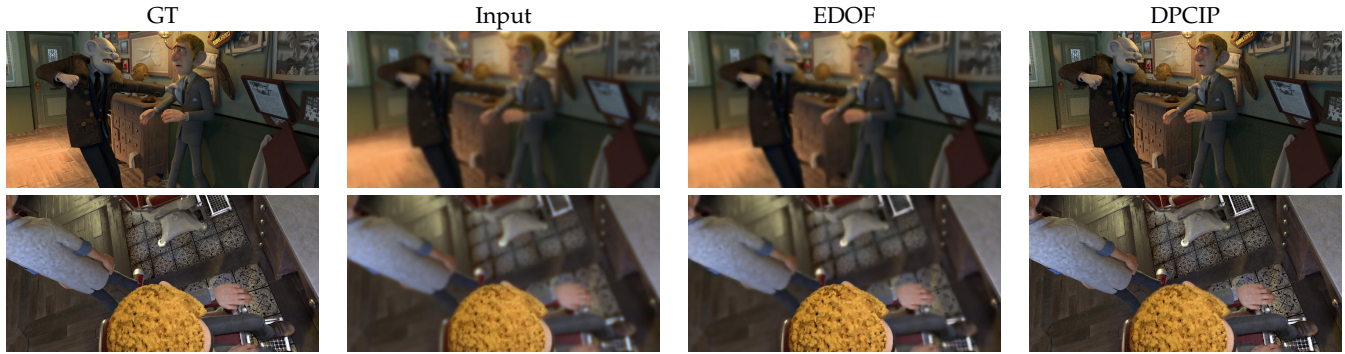


Fig. 3. **A qualitative comparison of image reconstruction.** Our method produced a much more accurate all-in-focus images, The existing baseline produced over-smooth all-in-focus images compared to our method.

#### 4.1.2 Extended Depth Of Field (EDOF)

To assess our method performance in the task of extended depth of field (EDOF) we compared ourselves to [7] which built upon the same phase-coded imaging system, we also follow the same optical parameters to produce the same acquired images. In this case, the original method was trained on a different synthetic dataset, so we could test on all the images in our subset. Table 2 shows a quantitative comparison in terms of PSNR and SSIM. Visual results can be found in Figure 3. Overall, our method outperformed the baseline by 5 dB in PSNR and 0.13 in SSIM on average and showed an improvement in terms of image reconstruction metrics, remarkably, relying only on a single given phase-coded image. Our method outperformed the previous supervised method [7] both in terms of PSNR [dB] and SSIM with the same imaging system. Table 2 shows a quantitative comparison using the agent subset. Qualitative results can be found in Figures 3, 8.

#### 4.1.3 Deblurring

We extend our experiments to solve blind image deblurring. The problem of image deblurring can be considered as a specific case of reconstructing an all-in-focus image from defocus where the full captured image is approximately at the same distance. We can simulate such a setup by taking images that the whole scene is above the physical distance of the camera, effectively causing the phase-coded imaging to collapse into a uniform convolution with a single PSF kernel.

For that purpose we also compared our method with Neural Deblurring [13], a similar approach that uses DIP as

a generator and a fully-connected network (FCN) to recover the sharp image and the blurring kernel respectively. For the purpose of deblurring we took from the ‘agent’ dataset 13 examples from 3 scenes. Each example has a constant depth map as described before.

However, Neural Deblurring fatally fails in scenarios where the deblurring kernel is large, and also when it’s channel dependent. Since comparing to Neural deblurring ‘out of the box’ is not really relevant, We adapt Neural Deblurring to work with our setup (e.g. phase mask kernel sizes), First we let it to predict each channel separately to match the models’ capacity to our problem. In addition, to overcome the kernel size limitation, we effectively reduced the predicted kernel from the original size of  $71 \times 71$  to  $19 \times 19$ . The reduction in size can be done since the pre-defined PSF kernels are centered.

In Table 3 we show a quantitative analysis of the signal coverage of reduced kernels from the full PSF kernels. In the trade-off between the energy loss of the PSF kernels and the ability of Neural Deblurring to converge, We chose kernel size of  $19 \times 19$  to predict on each channel independently and average the results to compare vs our method. Figure 4 demonstrates the deblurring improvement as a function of the reduction in kernel size.

To conclude our blind image deblurring experiments, Table 5 summarize our results quantitatively and Figures 5 and 9 demonstrate the results qualitatively for the deblurring case. Overall we can see that our method manages to outperform in blind image deblurring by effectively recovering a single valued depth map.

#### 4.1.4 Implicit generator effect

One of the key ideas of our method is the idea of considering DIP as an implicit model [1]. Since there has been a lot of work in the area of implicit neural representations (INR), we compared our method to several implicit models to see the effect of the generator type along with its positional input encoding. We conducted a study on the effect of the implicit generator. 15 images collected from 3 scenes were used as our test set. We tested three implicit generators: DIP [1], SIREN [39], and PIP [22] on both passive depth estimation and all-in-focus image reconstruction. Table 4 summarizes the implicit generator effect. Overall DIP outperformed both PIP and SIREN in terms of image reconstruction. In depth

TABLE 3

**PSF Kernel energy spread analysis.** Compared to the full signal, the Blue kernel is the most centered, while the Red kernel is the most spread out. We can see that reducing the kernel by half nearly effect the energy, but as we keep reducing the kernel size The loss of energy becomes severe.

Kernel size	R	G	B
71x71	100%	100%	100%
31x31	94.72%	96.69%	98.49%
23x23	87.31%	94.30%	97.32%
19x19	77.20%	89.10%	96.25%
15x15	56.24%	78.81%	94.28%

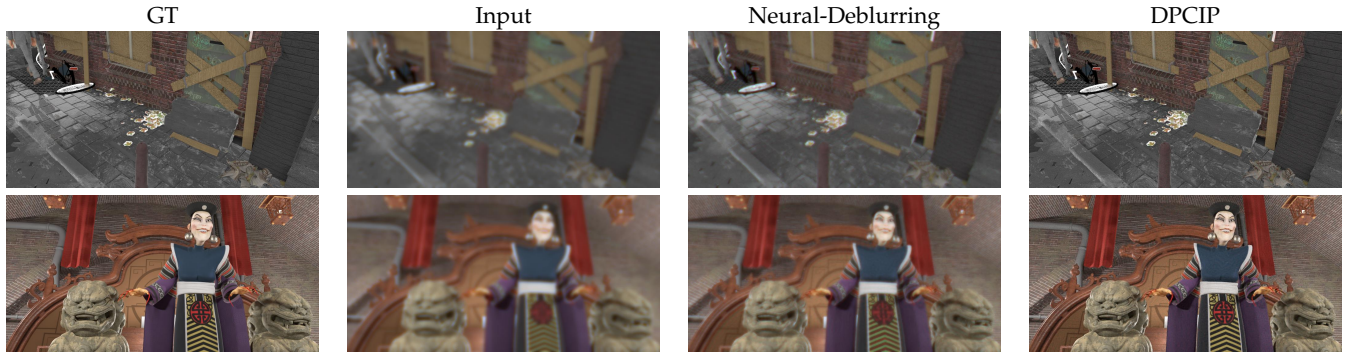


Fig. 5. **Image deblurring.** Our method outperforms Neural Deblurring. Even though we adapt Neural deblurring to be able to handle our deblurring subset, our method still outperforms by a significant margin, making it more usable for real-world applications where the PSF kernels can be large.

TABLE 4

**Generator effect.** We evaluated three types of generators in our method. DIP outperformed other generators in image reconstruction and was comparable to PIP in depth estimation. Both DIP and PIP outperformed SIREN in both tasks.

	DIP	PIP	SIREN
Depth Estimation (RMSE [m] ↓)	0.005	0.006	0.19
Image Reconstruction (PSNR / SSIM ↑)	30.15 / 0.916	26.34 / 0.82	25.85 / 0.81

estimation, PIP and DIP are comparable and they are both better than SIREN.

## 4.2 Real-World Results

We further extend our simulation results to real-world examples using a dedicated camera as done in [3], [4], [7]. For each image crop we compare ourselves to the relevant baseline in image reconstruction and passive depth estimation. Figures 6 and 10 summarize our results.

Interestingly, DIP which dominates in the simulation setup for all datasets and both tasks, is not working as well in the real-world setup. A possible hypothesis that can explain the results is that DIP is not as good as PIP at disentangling depth from texture, resulting in incorrect depth values and as a result, incorrect reconstruction.

In the simulated data there is less texture since we have no noise, thus the image is much more like a smooth depth map. To overcome the noise effect, we applied TV regularization to the estimated depth map to help the model produce a smoother depth map. The smoothness regularization helped achieve better depth maps but it is still not as good as PIP with the same regularization. When using PIP as our generator, we have more control over the smoothness by specifying an initialization scheme for the frequencies and limiting their bandwidth.

Overall, setting up the original settings (i.e. log-scale frequencies initializations and limiting the range as done in [22]) with TV regularization produced the best results.

## 5 CONCLUSION

In this work, we have proposed a self-supervised method for recovering an absolute depth map and an all-in-focus image using a phase-coded imaging system. As opposed to previous methods that rely on datasets for recovering the

depth map or the all-in-focus image, we do it solely on the given captured image and the knowledge of the optical setup by leveraging the image prior of implicit models.

Our method reduces the need for using training datasets since collecting such datasets can be hard and requires external graphics rendering software. Providing a solution for real-world setups and users who seek to use an existing imaging system without the need for any additional information or data other than optical parameters. In addition, due to the high quality of restoration, our method can provide “pseudo GT” to be used as supervision for training a neural network to restore an all-in-focus image from the blurred acquired image. This way we can enjoy both high quality of reconstruction and fast inference time.

TABLE 5

**Image deblurring.** Our method outperforms previous blind image deblurring works (even after the adaptation) both in PSNR [dB] and SSIM.

	Baseline [13]	DPCIP
Deblurring	19.6/0.67	26.38/0.834

## ACKNOWLEDGMENTS

This work was supported by the European research council under Grant ERC-StG 757497. This work was supported by Tel Aviv University Center for AI and Data Science (TAD).

## REFERENCES

- [1] D. Ulyanov, A. Vedaldi, and V. Lempitsky, “Deep image prior,” in *Proceedings of the IEEE conference on computer vision and pattern recognition*, 2018, pp. 9446–9454.
- [2] A. Levin, R. Fergus, F. Durand, and W. T. Freeman, “Image and depth from a conventional camera with a coded aperture,” *ACM transactions on graphics (TOG)*, vol. 26, no. 3, pp. 70–es, 2007.
- [3] H. Haim, S. Elmalem, R. Giryes, A. M. Bronstein, and E. Marom, “Depth estimation from a single image using deep learned phase coded mask,” *IEEE Transactions on Computational Imaging*, vol. 4, no. 3, pp. 298–310, 2018.
- [4] Y. Gil, S. Elmalem, H. Haim, E. Marom, and R. Giryes, “Online training of stereo self-calibration using monocular depth estimation,” *IEEE Transactions on Computational Imaging*, vol. 7, pp. 812–823, 2021.
- [5] J. Chang and G. Wetzstein, “Deep optics for monocular depth estimation and 3d object detection,” in *Proceedings of the IEEE/CVF International Conference on Computer Vision*, 2019, pp. 10 193–10 202.



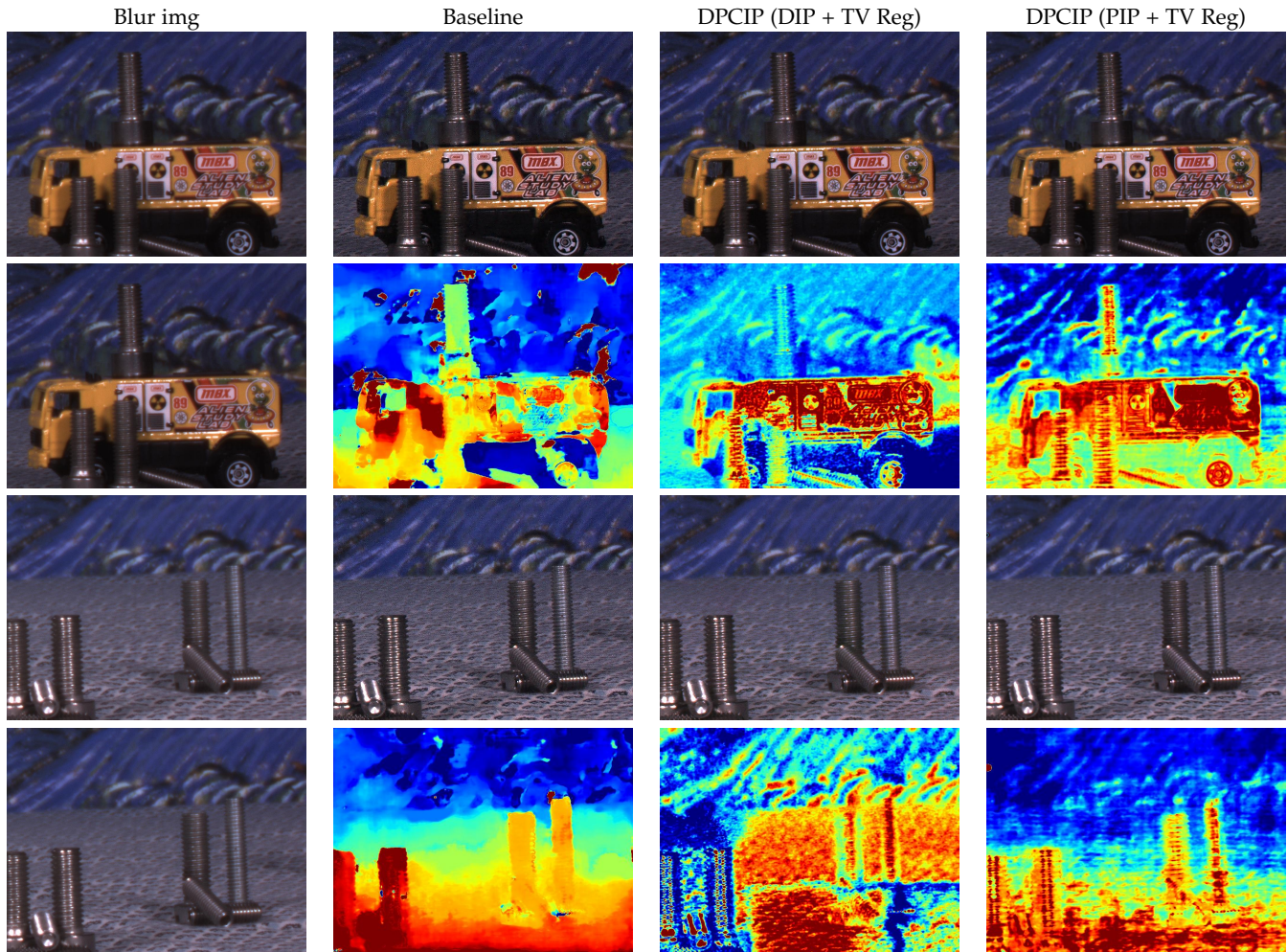


Fig. 6. **Real world examples.** We can see that using PIP as the generator generates the most accurate depth maps and also the best all-in-focus images. Using DIP as a generator tends to produce too detailed depth maps, but with good all-in-focus images, this means that PIP as a generator disentangle better between the depth map estimation and the all-in-focus restoration. In all cases, previous baselines produced worse outputs compare to our method. depth maps are over-smoothed and all-in-focus images are a bit noiser than ours.

- [6] Y. Wu, V. Boominathan, H. Chen, A. Sankaranarayanan, and A. Veeraraghavan, "Phasecam3d — learning phase masks for passive single view depth estimation," in *2019 IEEE International Conference on Computational Photography (ICCP)*, 2019, pp. 1–12.
- [7] S. Elmalem, R. Giryes, and E. Marom, "Learned phase coded aperture for the benefit of depth of field extension," *Optics express*, vol. 26, no. 12, pp. 15 316–15 331, 2018.
- [8] U. Akpinar, E. Sahin, M. Meem, R. Menon, and A. Gotchev, "Learning wavefront coding for extended depth of field imaging," *IEEE Transactions on Image Processing*, vol. 30, pp. 3307–3320, 2021.
- [9] I. Gkioulekas, J. Chen, J. T. Barron, N. Wadhwa, P. Srinivasan, R. Garg, S. Xin, and T. Xue, "Defocus map estimation and blur removal from a single dual-pixel image," 2021.
- [10] V. Sitzmann, S. Diamond, Y. Peng, X. Dun, S. Boyd, W. Heidrich, F. Heide, and G. Wetzstein, "End-to-end optimization of optics and image processing for achromatic extended depth of field and super-resolution imaging," *ACM Transactions on Graphics (TOG)*, vol. 37, no. 4, pp. 1–13, 2018.
- [11] E. Yosef, S. Elmalem, and R. Giryes, "Video reconstruction from a single motion blurred image using learned dynamic phase coding," *arXiv preprint arXiv:2112.14768*, 2021.
- [12] Y. Gandelsman, A. Shocher, and M. Irani, "double-dip": unsupervised image decomposition via coupled deep-image-priors," in *Proceedings of the IEEE/CVF Conference on Computer Vision and Pattern Recognition*, 2019, pp. 11 026–11 035.
- [13] D. Ren, K. Zhang, Q. Wang, Q. Hu, and W. Zuo, "Neural blind deconvolution using deep priors," in *Proceedings of the IEEE/CVF Conference on Computer Vision and Pattern Recognition*, 2020, pp. 3341–3350.
- [14] T. Yokota, K. Kawai, M. Sakata, Y. Kimura, and H. Hontani, "Dynamic pet image reconstruction using nonnegative matrix factorization incorporated with deep image prior," in *Proceedings of the IEEE/CVF International Conference on Computer Vision (ICCV)*, October 2019.
- [15] F. Hashimoto, K. Ote, and Y. Onishi, "PET image reconstruction incorporating deep image prior and a forward projection model," *IEEE Transactions on Radiation and Plasma Medical Sciences*, vol. 6, no. 8, pp. 841–846, nov 2022. [Online]. Available: <https://doi.org/10.1109%2Ftrpms.2022.3161569>
- [16] K. Gong, C. Catana, J. Qi, and Q. Li, "Pet image reconstruction using deep image prior," *IEEE Transactions on Medical Imaging*, vol. 38, no. 7, pp. 1655–1665, 2019.
- [17] —, "Direct reconstruction of linear parametric images from dynamic pet using nonlocal deep image prior," *IEEE Transactions on Medical Imaging*, vol. 41, no. 3, pp. 680–689, 2022.
- [18] G. Mataev, M. Elad, and P. Milanfar, "Deepred: Deep image prior powered by red," *ArXiv*, vol. abs/1903.10176, 2019.
- [19] R. Fermanian, M. Le Pendu, and C. Guillemot, "Regularizing the Deep Image Prior with a Learned Denoiser for Linear Inverse Problems," in *MMSp 2021 - IEEE 23rd International Workshop on Multimedia Signal Processing*. Tampere, Finland: IEEE, Oct. 2021, pp. 1–6. [Online]. Available: <https://hal.archives-ouvertes.fr/hal-03310533>
- [20] E. Kurniawan, Y. Park, and S. Lee, "Noise-resistant demosaicing with deep image prior network and random rgbw color filter array," *Sensors*, vol. 22, no. 5, p. 1767, 2022.
- [21] Y.-C. Chen, C. Gao, E. Robb, and J.-B. Huang, "Nas-dip: Learning deep image prior with neural architecture search," in *European*

- Conference on Computer Vision*. Springer, 2020, pp. 442–459.
- [22] N. Shabtay, E. Schwartz, and R. Giryes, “Pip: Positional-encoding image prior,” *arXiv preprint arXiv:2211.14298*, 2022.
- [23] M. Tancik, P. Srinivasan, B. Mildenhall, S. Fridovich-Keil, N. Raghavan, U. Singhal, R. Ramamoorthi, J. Barron, and R. Ng, “Fourier features let networks learn high frequency functions in low dimensional domains,” *Advances in Neural Information Processing Systems*, vol. 33, pp. 7537–7547, 2020.
- [24] B. Mildenhall, P. P. Srinivasan, M. Tancik, J. T. Barron, R. Ramamoorthi, and R. Ng, “Nerf: Representing scenes as neural radiance fields for view synthesis,” in *Computer Vision—ECCV 2020: 16th European Conference, Glasgow, UK, August 23–28, 2020, Proceedings, Part I*, 2020, pp. 405–421.
- [25] V. Sitzmann, J. N. Martel, A. W. Bergman, D. B. Lindell, and G. Wetzstein, “Implicit neural representations with periodic activation functions,” in *arXiv*, 2020.
- [26] A. Yu, R. Li, M. Tancik, H. Li, R. Ng, and A. Kanazawa, “Plenoc-trees for real-time rendering of neural radiance fields,” in *Proceedings of the IEEE/CVF International Conference on Computer Vision (ICCV)*, October 2021, pp. 5752–5761.
- [27] J. T. Barron, B. Mildenhall, D. Verbin, P. P. Srinivasan, and P. Hedman, “Zip-nerf: Anti-aliased grid-based neural radiance fields,” *arXiv preprint arXiv:2304.06706*, 2023.
- [28] T. Müller, A. Evans, C. Schied, and A. Keller, “Instant neural graphics primitives with a multiresolution hash encoding,” *ACM Transactions on Graphics (ToG)*, vol. 41, no. 4, pp. 1–15, 2022.
- [29] J. T. Barron, B. Mildenhall, M. Tancik, P. Hedman, R. Martin-Brualla, and P. P. Srinivasan, “Mip-nerf: A multiscale representation for anti-aliasing neural radiance fields,” in *Proceedings of the IEEE/CVF International Conference on Computer Vision (ICCV)*, October 2021, pp. 5855–5864.
- [30] J. T. Barron, B. Mildenhall, D. Verbin, P. P. Srinivasan, and P. Hedman, “Mip-nerf 360: Unbounded anti-aliased neural radiance fields,” in *Proceedings of the IEEE/CVF Conference on Computer Vision and Pattern Recognition (CVPR)*, June 2022, pp. 5470–5479.
- [31] M. Tancik, V. Casser, X. Yan, S. Pradhan, B. Mildenhall, P. P. Srinivasan, J. T. Barron, and H. Kretschmar, “Block-nerf: Scalable large scene neural view synthesis,” in *Proceedings of the IEEE/CVF Conference on Computer Vision and Pattern Recognition (CVPR)*, June 2022, pp. 8248–8258.
- [32] A. Yu, V. Ye, M. Tancik, and A. Kanazawa, “pixelnerf: Neural radiance fields from one or few images,” in *Proceedings of the IEEE/CVF Conference on Computer Vision and Pattern Recognition*, 2021, pp. 4578–4587.
- [33] B. Mildenhall, P. Hedman, R. Martin-Brualla, P. P. Srinivasan, and J. T. Barron, “Nerf in the dark: High dynamic range view synthesis from noisy raw images,” in *Proceedings of the IEEE/CVF Conference on Computer Vision and Pattern Recognition (CVPR)*, June 2022, pp. 16 190–16 199.
- [34] S. Ramasinghe and S. Lucey, “Beyond periodicity: towards a unifying framework for activations in coordinate-mlps,” in *Computer Vision—ECCV 2022: 17th European Conference, Tel Aviv, Israel, October 23–27, 2022, Proceedings, Part XXXIII*. Springer, 2022, pp. 142–158.
- [35] A. Hertz, O. Perel, R. Giryes, O. Sorkine-Hornung, and D. Cohen-Or, “Sape: Spatially-adaptive progressive encoding for neural optimization,” *Advances in Neural Information Processing Systems*, vol. 34, pp. 8820–8832, 2021.
- [36] D. B. Lindell, D. Van Veen, J. J. Park, and G. Wetzstein, “Bacon: Band-limited coordinate networks for multiscale scene representation,” in *CVPR*, 2022.
- [37] Z. Wang, A. C. Bovik, H. R. Sheikh, and E. P. Simoncelli, “Image quality assessment: from error visibility to structural similarity,” *IEEE transactions on image processing*, vol. 13, no. 4, pp. 600–612, 2004.
- [38] D. P. Kingma and J. Ba, “Adam: A method for stochastic optimization,” *arXiv preprint arXiv:1412.6980*, 2014.
- [39] V. Sitzmann, J. Martel, A. Bergman, D. Lindell, and G. Wetzstein, “Implicit neural representations with periodic activation functions,” *Advances in Neural Information Processing Systems*, vol. 33, pp. 7462–7473, 2020.



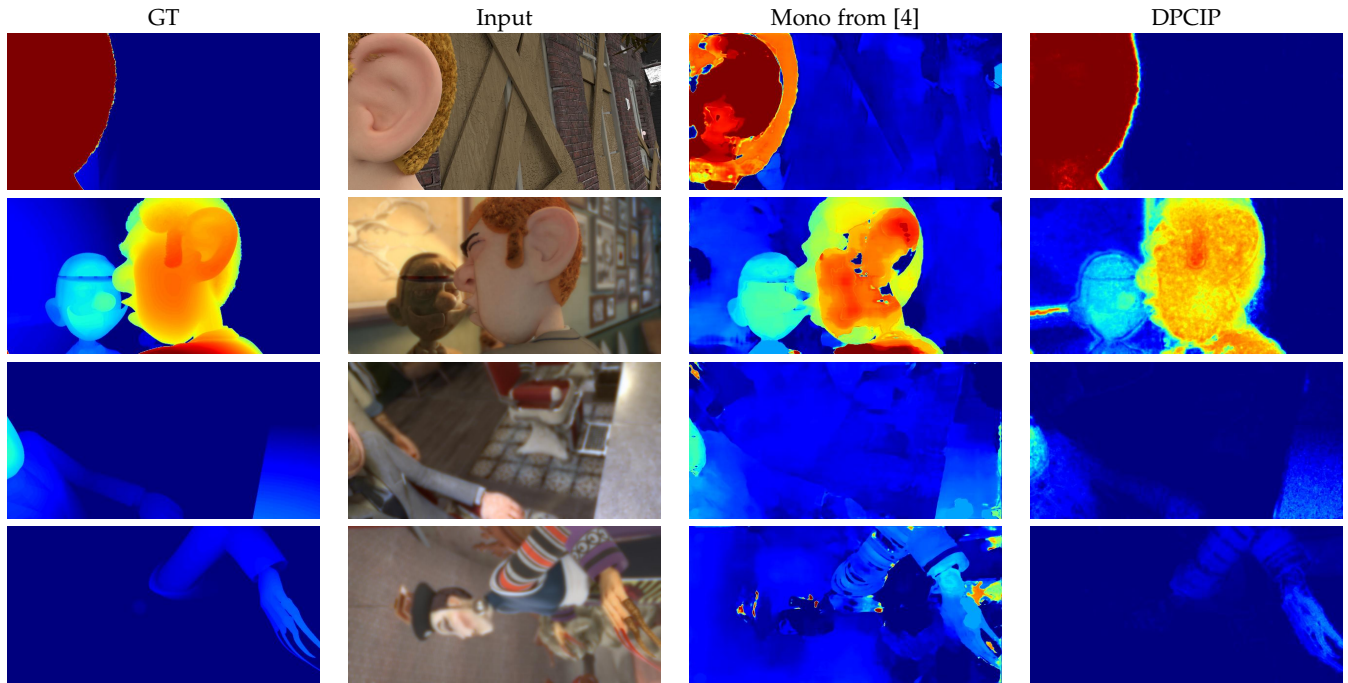


Fig. 7. **Depth Estimation visual examples.** DPCIP produced more accurate depth maps, even on scenes the mono network was trained on. Note that the depths are clipped to the physical range of the imaging system.

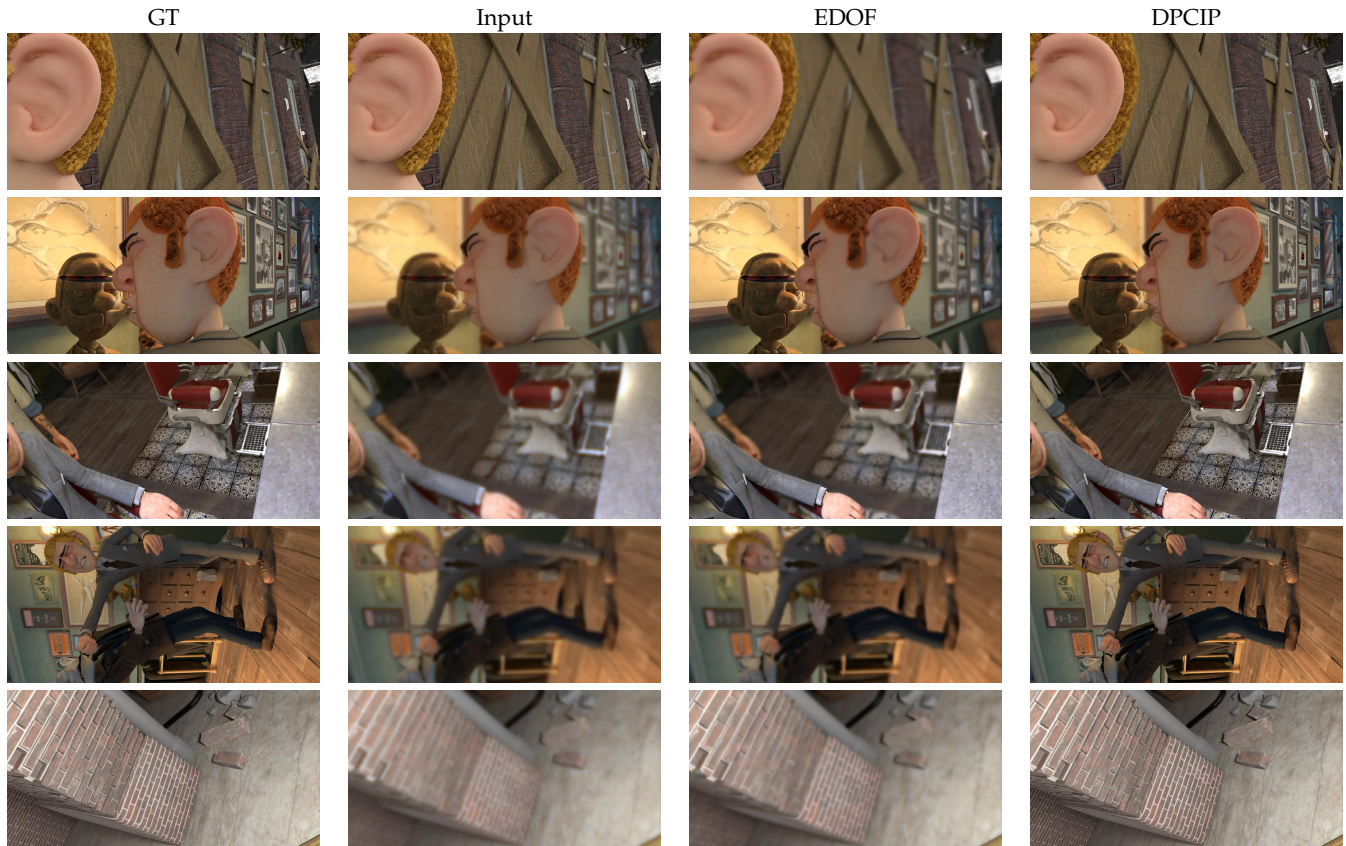


Fig. 8. **All-in-Focus Image Reconstruction visual examples.** An example from each scene. Our method outperforms the baseline and produced significantly higher quality reconstruction.



Fig. 9. **Image Deblurring visual examples.** Our method produces an accurate sharp images, and is also capable of handling large blurring kernels while SelfDeblur struggles.



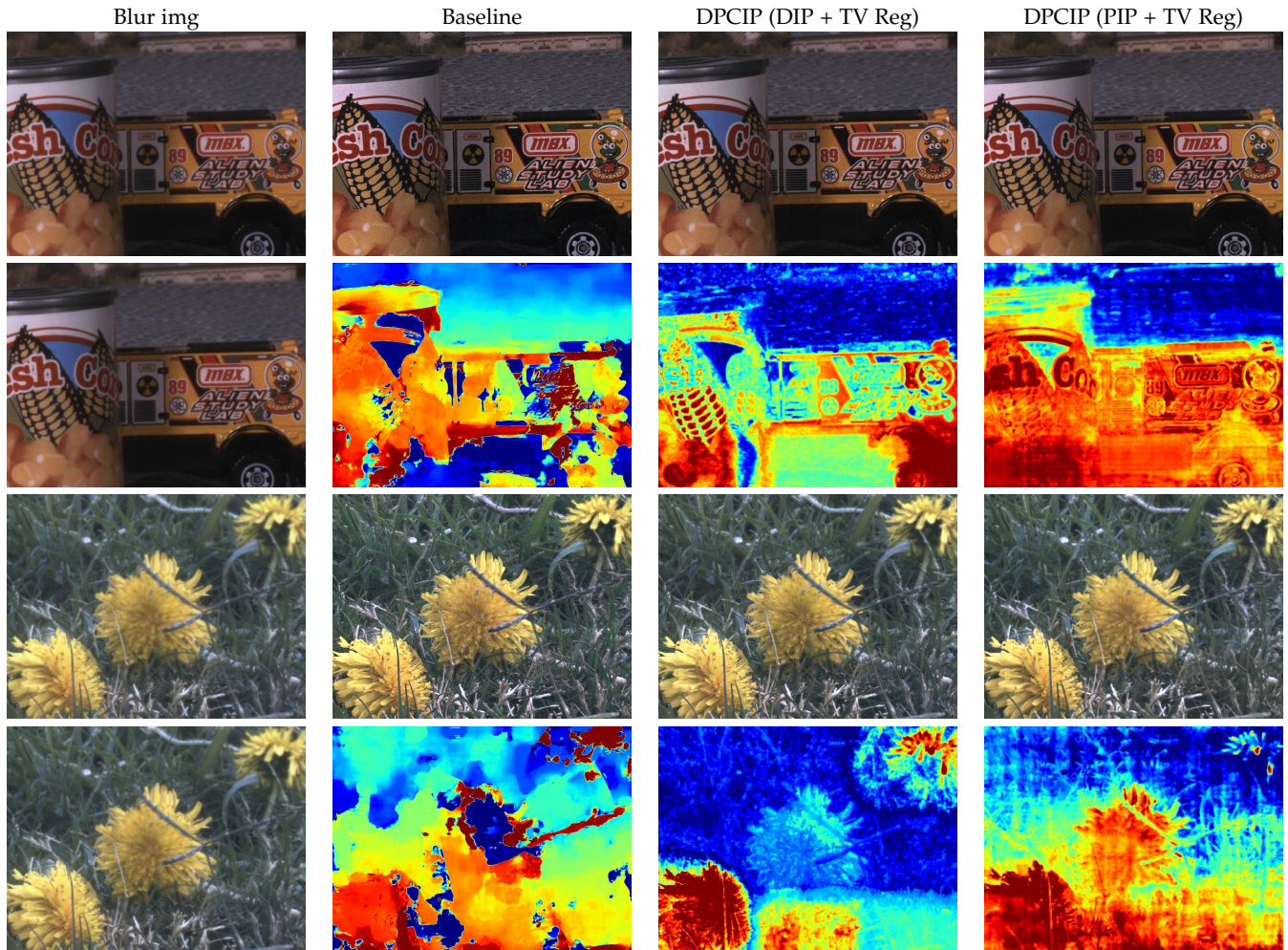


Fig. 10. Real world qualitative examples. DPCIP produced higher quality reconstruction images and depth maps compared to the baselines.